RESEARCH ARTICLE

Rising Stars

ADVANCED MATERIALS
www.advmat.de

Direct Laser Processing and Functionalizing PI/PDMS Composites for an On-Demand, Programmable, Recyclable Device Platform

Jia Zhu, Yang Xiao, Xianzhe Zhang, Yao Tong, Jiaying Li, Ke Meng, Yingying Zhang, Jiuqiang Li, Chenghao Xing, Senhao Zhang, Benkun Bao, Hongbo Yang, Min Gao, Taisong Pan, Shangbin Liu, Farnaz Lorestani, Huanyu Cheng,* and Yuan Lin**

Skin-interfaced high-sensitive biosensing systems to detect electrophysiological and biochemical signals have shown great potential in personal health monitoring and disease management. However, the integration of 3D porous nanostructures for improved sensitivity and various functional composites for signal transduction/processing/transmission often relies on different materials and complex fabrication processes, leading to weak interfaces prone to failure upon fatigue or mechanical deformations. The integrated system also needs additional adhesive to strongly conform to the human skin, which can also cause irritation, alignment issues, and motion artifacts. This work introduces a skin-attachable, reprogrammable, multifunctional, adhesive device patch fabricated by simple and low-cost laser scribing of an adhesive composite with polyimide powders and amine-based ethoxylated polyethylenimine dispersed in the silicone elastomer. The obtained laser-induced graphene in the adhesive composite can be further selectively functionalized with conductive nanomaterials or enzymes for enhanced electrical conductivity or selective sensing of various sweat biomarkers. The possible combination of the sensors for real-time biofluid analysis and electrophysiological signal monitoring with RF energy harvesting and communication promises a standalone stretchable adhesive device platform based on the same material system and fabrication process.

1. Introduction

Capable of directly interfacing with soft and irregular human tissues, flexible electronics can monitor relevant physiological conditions in a non-invasive manner for personal health management and clinical applications.[1] The fabrication of various functional components (e.g., sensors, electrodes, and interconnects) on pliable substrates for flexible electronics largely relies on photolithography, transfer printing, or direct printing.[2] However, these fabrication techniques either require masks for patterning or specific nanomaterials (e.g., viscosity and surface energy of inks) for printing, which are often associated with high complexity and cost. As an alternative approach, mask-free laser fabrication holds great potential in the mass fabrication of flexible electronics due to its high precision, efficiency, and low cost.[1d] Porous conductive 3D graphene networks induced by laser scribing of carbon-rich polymers, or laser-induced graphene (LIG), provide a

J. Zhu, Y. Xiao, J. Li, K. Meng, M. Gao, T. Pan, Y. Lin
School of Material and Energy
University of Electronic Science and Technology of China
Chengdu 610054, China
E-mail: linyuan@uestc.edu.cn

J. Zhu
Yangtze Delta Region Institute (Quzhou)
University of Electronics Science and Technology of China
Quzhou 324000, China

J. Zhu, X. Zhang, C. Xing, S. Liu, F. Lorestani, H. Cheng
Department of Engineering Science and Mechanics
The Pennsylvania State University
University Park, PA 16802, USA
E-mail: fkl5072@psu.edu; Huanyu.Cheng@psu.edu

Y. Tong, Y. Zhang, J. Li, S. Zhang, B. Bao, H. Yang
Suzhou Institute of Biomedical Engineering and Technology
Chinese Academy of Science
Suzhou 215011, P. R. China

Y. Lin
Medico-Engineering Cooperation on Applied Medicine Research Center
University of Electronics Science and Technology of China
Chengdu 610054, China

The ORCID identification number(s) for the author(s) of this article can be found under https://doi.org/10.1002/adma.202400236

DOI: 10.1002/adma.202400236

large specific surface area for chemical or electrochemical sensing.[3] Sensing materials can be decorated on the LIG network by dip-coating or chemical reduction from precursors by second laser scribing.[3b] Successful demonstrations based on this strategy include modifications with MoS_2 or metal oxides for gas sensing,[3b] Ni/Au coplating for nonenzymatic glucose sensing,[4] and cobalt oxide doping for supercapacitors.[5] However, these sensors and devices built on flexible substrates are not intrinsically stretchable and cannot conformally interface with the irregular human skin for bio-sensing. Although LIG can be transferred to stretchable elastomers, the infiltration of elastomer precursors into the porous structure greatly reduces the porosity, specific surface area, and hydrophilicity of the LIG network.[6] As a result, it is also challenging to carry out subsequent doping and the sensing performance is degraded. To address these challenges, it is highly desirable to prepare porous 3D LIG directly on the stretchable substrate. Although a stretchable LIG supercapacitor is fabricated from the polyvinyl alcohol/polyimide (PVA/PI) composite,[7] this platform is not able to interface with human skin/tissues for biosensing due to the water solubility of PVA.

In most cases, separate fabrication processes are needed for sensors, data transmission units, power supply, or energy harvesting modules, and electrical interconnects, which are further hetero-integrated into a flexible device platform.[8] Besides challenges in device miniaturization, mechanical mismatch introduced at the interface often results in compromised durability. Therefore, tremendous attention has been paid to exploiting the same material system or process for fabricating device platforms.[9] For example, the silver nanofiller/polydimethylsiloxane (PDMS) composites with different nanofiller dimensions and their combinations can change the strain-dependent conductivity for strain sensing or electrical interconnects.[9c] Conjugating Ag nanowire (AgNW) nanofillers with surface ligands in the composite leads to better strain-insensitivity of the composite due to the adaptive self-organizations under stretching. With the introduction of additional Ag nanoparticles (AgNPs, 30 wt%) and Ag nanoflakes (AgNFs, 30 wt%), the resistance change of the composite reduces to 0.26% under 50% stretching. Combining AgNW-based strain-sensitive with AgNW/AgNP/AgNF-based strain-insensitive composite as the sensing and interconnections yields a stretchable system for precise local strain sensing. However, the preparation process using a large amount of noble metal nanomaterials is relatively complex and expensive and the simple tuning of the conductivity shows limited application opportunities. In comparison, the single LIG/MXenes material system with high chemical or electrochemical reactivity is used to fabricate a standalone stretchable gas sensing system consisting of a triboelectric nanogenerator, power management circuit, microsupercapacitor array, and gas sensors.[9a] Even though different structural designs (e.g., the 3D buckling and island-bridge structure) have been used to improve the overall stretchability, the standalone sensing system is not compact and has very limited attachability due to the lack of adhesion.

To the best of our knowledge, low-cost and efficient fabrication of multifunctional skin-interfaced electronics with intrinsic adhesion on a single material platform is still lacking. This work exploits direct laser patterning and postmodifications of a stretchable adhesive composite based on polyimide (PI) powders in PDMS with amine-based polyethylenimine ethoxylated (PEIE) additives for varying functional device units. The resulting porous 3D LIG network on the stretchable adhesive patch from laser patterning allows facile subsequent selective postmodifications to provide electrical connections or serve as active sensing units or device components. Due to the intrinsic adhesion contributed by PEIE that modifies the crosslinking density of PDMS, the demonstrated biosensors can provide real-time and high-fidelity monitoring of physiological signals such as electrocardiogram/electromyography (ECG/EMG) or molecular-level sweat biomarkers (e.g., glucose and lactic). The laser-written LIG patterns can also be simply erased by taping and rewriting the LIG composite features great reusability and reconfigurability. The seamless and compact integration of these modules affords multifunctional device-level platforms for real-time monitoring and controllable drug delivery to enable a closed-loop system, which holds great potential in disease diagnostics and treatment evaluation, such as chronic wounds and diabetes.

2. Results and Discussion

2.1. Design Strategy of LIG@PI/PDMS/PEIE

The stretchable bioadhesive composite is designed by mixing PI powders (size of ≈6 µm) with PDMS precursors and PEIE additive followed by curing at 80 °C for 3 h (**Figure** 1a). The PI microparticles and PDMS serve as the functional component and supporting matrix, respectively, whereas the PEIE additives provide enhanced adhesion by forming a complex with Pt catalyst in PDMS to reduce its crosslinking density.[10] Similar enhanced adhesive strength of PDMS can be achieved by adding polyethylene glycol (PEG).[11] Upon laser scribing, PI microparticles are carbonized to form conductive porous 3D LIG patterns through a liquefaction process arising from a photothermal reaction, whereas PDMS is converted into semiconducting silicon carbide or silica, depending on the environment.[7b,12] Different from the LIG created from the PI film (LIG@PI), the LIG fabricated from the adhesive composite (LIG@PI/PDMS/PEIE) exhibits good stretchability and strong adhesion to directly form conformal contact with human skin. Although stretchability and adhesion can be slightly improved after transferring LIG@PI to PDMS (LIG@PDMS) through an infiltration and separation process, the PDMS on the LIG network significantly reduces the porous structures and postprocessability (e.g., coating or functionalization). As a result, LIG@PI/PDMS/PEIE combines and exceeds the figure-of-merits of both LIG@PI and LIG@PDMS to open up additional application opportunities in bioelectronics (Figure 1b; and Table S1, Supporting Information). With on-demand laser scribing and facile postfunctionalization, the adhesive multifunctional skin-interfaced device platform can be fabricated to measure biopotential and other physiologically relevant chemical signals, provide electrical stimulations and drug delivery, and integrate wireless modules for future data/energy transmission (Figure 1c). The postfunctionalization of the LIG@PI/PDMS/PEIE composite with specific enzymes (or aptamers) provides highly sensitive and selective electrochemical

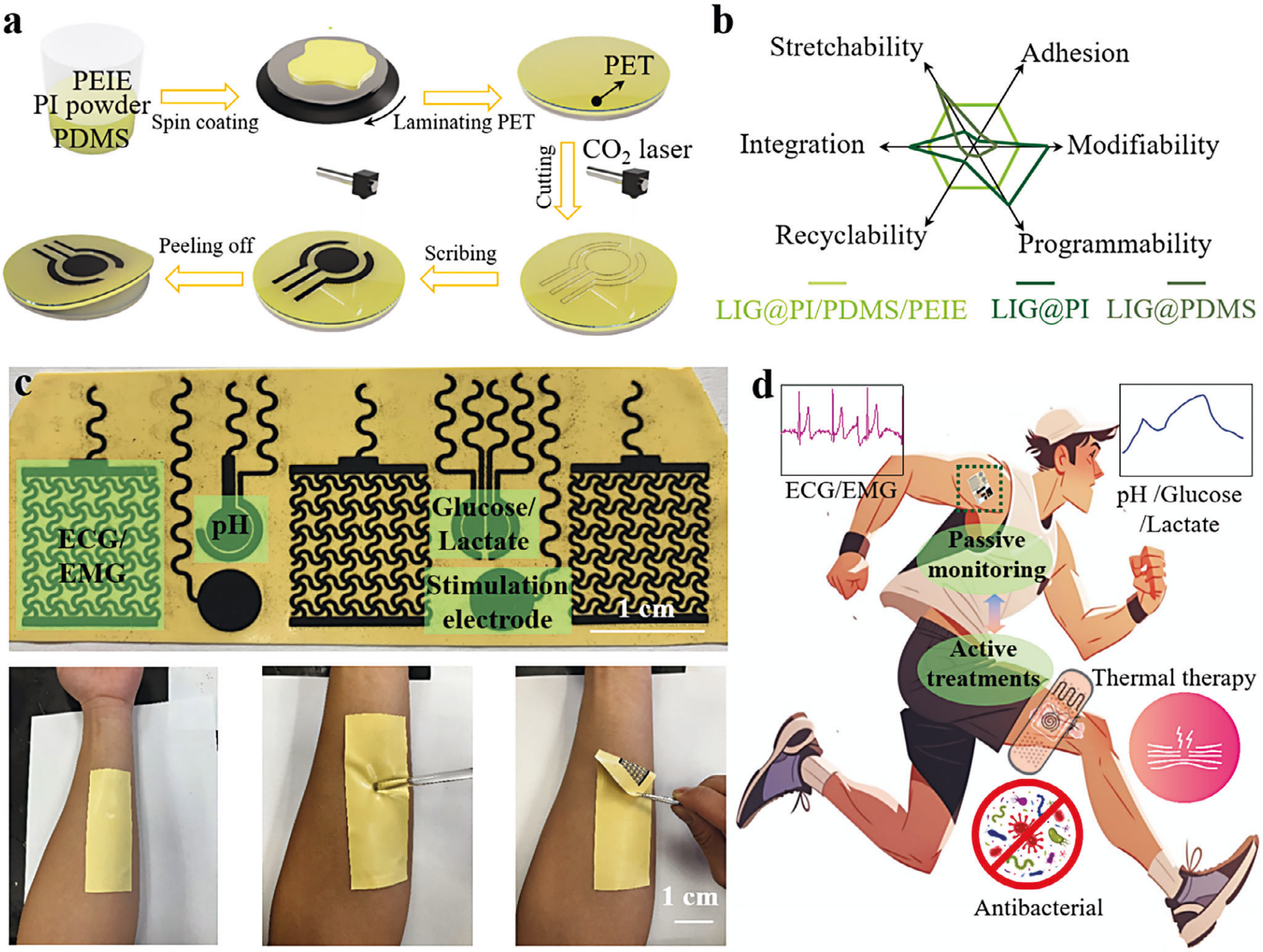

Figure 1. LIG@PI/PDMS/PEIE-based multifunctional, recyclable, and adhesive device patch. a) Schematics illustrating the fabrication process of the PI/PDM/PEIE-based device patch. b) Radar chart of various LIG forms, including that derived from the PI/PDMS/PEIE composite (LIG@PI/PDMS/PEIE), or the PI film (LIG@PI), and transferred to PDMS (LIG@PDMS). c) Optical images of a PI/PDM/PEIE-based patch for biopotential regulation and measurement, and biosensing. The bottom panel shows the multifunction device patch being attached to skins, under deformations induced by poking, and during peeling off. d) Schematics showing the multifunctional LIG@PI/PDMS/PEIE-based adhesive device patch with biopotential measurement, electrical stimulation, biosensing, thermal management, and wound treatment capabilities.

sensors toward biomarkers, such as pH, glucose and lactate. The highly conductive nanomaterials decorated on the composite allow for motion-artifact-free electrophysiological signal monitoring, efficient joule heating toward thermal therapy, and low-loss RF circuits for wireless communication or powering (Figure 1d). Additionally, simple erasing with peeling off and rewriting with the same laser setup showcase a unique yet efficient fabrication platform to create recyclable and reusable flexible sensors and devices with incomparable programmability at low cost.

2.2. Optimization of Mechanical Stiffness, Adhesion, and Electrical Properties of LIG@PI/PDMS/PEIE

PEIE can greatly reduce the crosslinking density of PDMS for enhanced adhesion. As a result, the strong yet tunable adhesive strength of the PI/PDMS/PEIE composite to target surfaces can be easily modulated by changing the PEIE content. With a customized experimental setup, the adhesion of the PI/PDMS/PEIE composite to a glass slide before LIG preparation is experimentally measured during the peeling-off process with the adhesive strength extracted from the plateau of the normalized force per unit width versus time curve (Figure S1, Supporting Information). For the PI/PDMS composite with a mixing weight ratio of 0.5:1 (i.e., PI$_{0.5}$/PDMS), the adhesion increases significantly from 0.164 to 63.377 N m^{-1} as the PEIE content increases from 15 to 30 μL per 10 g PDMS (**Figure 2a**). It should be noted that the adhesion of PI/PDMS/PEIE decreases after laser scribing as the created LIG in LIG@PI/PDMS/PEIE is nonadhesive. At the same time, Young's modulus (calculated from the slope of the strain–stress curve in Figure S2, Supporting Information) of the resulting composite also decreases from 0.70 to 0.11 MPa due to the incorporation of PEIE (Figure 2b). However, the reduced modulus may not provide sufficient cohesion to maintain the integrity of LIG

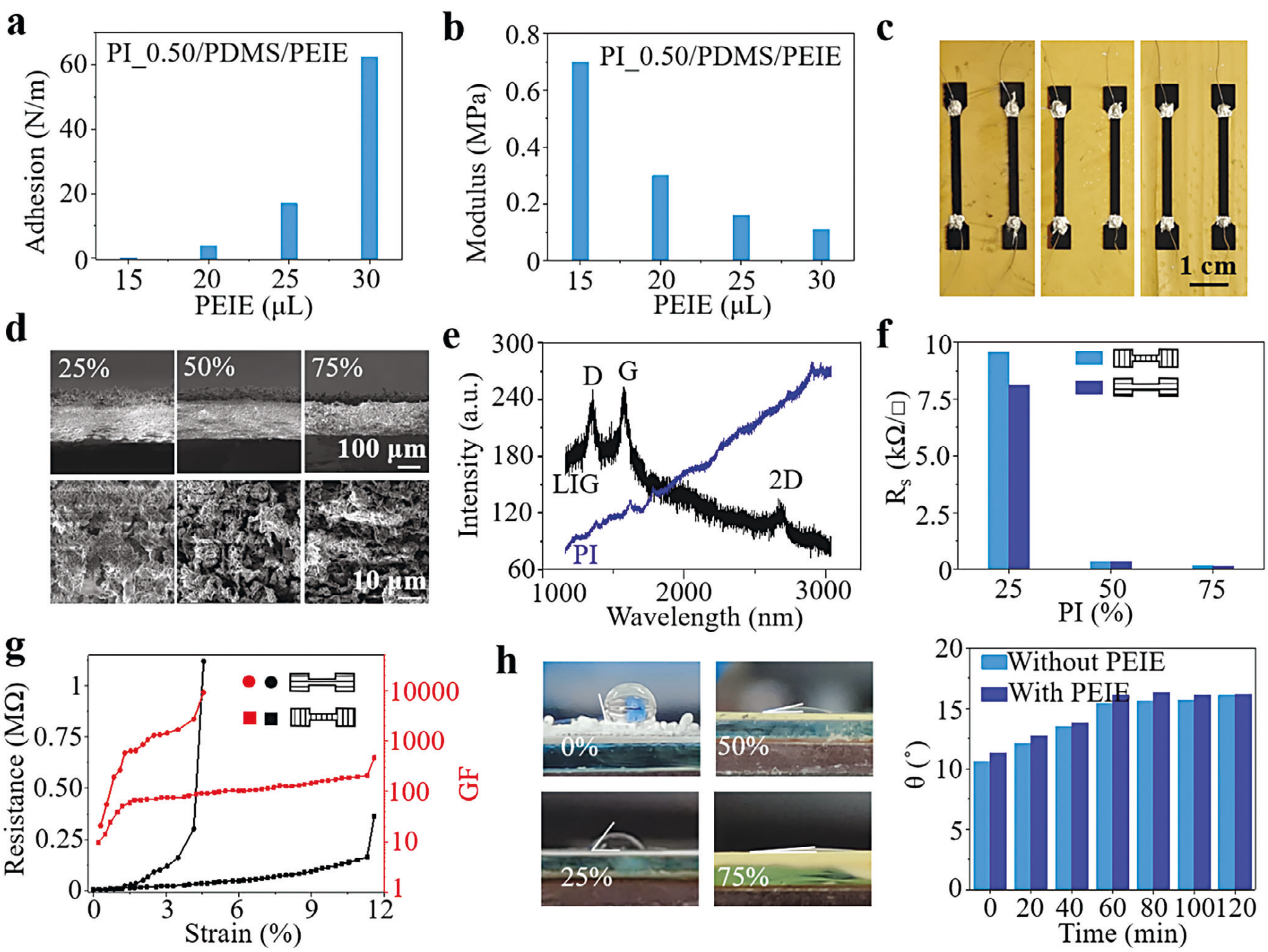

Figure 2. Mechanical and electrical characterization of the PI/PDMS/PEIE composite and materials characterization of LIG fabricated from the composite. Adhesion strength a) and modulus b) of the PI/PDMS composite with varying PEIE additives. c) Optical images of the PI/PDMS/PEIE composite with different PI fractions (i.e., 20%, 50%, and 75%) and the as-fabricated LIG. d) SEM images and e) Raman spectrum of LIG fabricated from the adhesive PI/PDMS/PEIE composite. f) Measured sheet resistance of LIG fabricated from the PI/PDMS/PEIE composite with different PI fractions and laser scribing directions (i.e., longitudinal or transverse). g) Electromechanical response of LIG fabricated from the PI_0.5/PDMS composite with longitudinal or transverse laser scribing. h) Hydrophilicity of LIG fabricated from the PI_0.5/PDMS/PEIE composite with different PI fractions and the contact angle of LIG fabricated from the PI_0.5/PDMS/PEIE composite as a function of time.

patterns during peeling-off. As a result, it is important to co-optimize Young's modulus and adhesion of the PI/PDMS/PEIE composite.

The inherently nonstretchable and nonadhesive PI powders in the composite also modulate the mechanical properties of the composite by providing mechanical reinforcement and reducing the PDMS network density. The modulus of the adhesive PDMS/PEIE without PI powders is less than 0.1 MPa, which is significantly lower than the pristine PDMS (Figure S3a, Supporting Information). With 25% PI powders (to PDMS), the modulus is increased to 0.95 MPa which is even higher than the pristine PDMS, attributing to the reinforcing effect of stiff PI microparticles. However, further increasing PI content to 50% and 75% leads to a slightly reduced modulus of 0.21 and 0.11 MPa, which is consistent with the trend reported in previous work.[13] Since there are no direct interactions between PI microparticles, reduced modulus with overloading PI microparticles arises from the low PDMS density in the composite. Compared with PDMS without PI powders (PDMS/PEIE), only the one with 50% PI powders (PI_0.50/PDMS/PEIE) shows a slight improvement of 24% in the adhesive strength (Figure S3b, Supporting Information). As a result, the content of both the PI and PEIE can be leveraged to tune the adhesive strength and modulus of the resulting composite. Additionally, the optical reflection of the composite diminishes with the increasing PI content, which results in distinct visual appearances (Figure 2c). Using the same constituent materials and fabrication process can also prepare elastomeric substrates with spatial-dependent mechanical properties and LIG patterns with tunable electrical properties. Meanwhile, highly permeable LIG@PI/PDMS/PEIE can be prepared by adding volatile ethanol into the precursor to introduce porous structures (Figure S4, Supporting Information). The porous structure leads to a threefold increase in water permeability (≈0.003 g cm^{-2} h^{-1}) that is comparable to textile-based electronics

(≈0.004 g cm^{-2} h^{-1}),[14] allowing applications in skin-interfaced electronics.

The pristine PDMS is mainly converted to microstructured silica during laser scribing in the ambient environment. The use of PI powders in the composite changes coarse and discontinuous flakes induced by laser scribing to continuous and porous LIG networks, as revealed by the SEM images (Figure 2d). The porosity of the resulting LIG increases with the increasing PI powders, culminating in an average pore size of ≈10 µm for 75% PI powders, which is much larger than that of LIG@PI.[4] This is due to the lower PI fraction in the PI/PDMS composite than the PI film and the partial block by the non-converted PDMS. Different from the pristine PI/PDMS substrate, the as-fabricated LIG shows three characteristic peaks of graphene at 1356 (D), 1580 (G), and 2700 (2D) cm^{-1} in the Raman spectrum (Figure 2e), which confirms the formation of few-layered LIG as in the previous study.[4] The ratio of the 2D to G peak of ≈0.3 indicates the existence of multilayered graphene. The disorders or defects of porous graphene revealed by the D peak provide active sites for sensing. These results confirm the successful conversion from PI particles in the composite to multilayered porous graphene by laser scribing.[15]

The morphology and electrical properties of the resulting LIG fabricated from the PI/PDMS/PEIE composite primarily determined by the PI content are revealed by the electrical and electromechanical characterizations of dogbone-shaped patterns. The laser parameters with an image density of 6 (i.e., 1000 lines per inch) and laser power of 10.5% are optimized to result in improved conductivity of the LIG (Figure S5, Supporting Information). LIG patterns with longitudinal laser scribing have lower sheet resistance than the transversely laser-scribed ones. For example, the sheet resistance (0.175 kΩ □$^{-1}$) of the longitudinally scribed LIG is lower than that (0.22 kΩ □$^{-1}$) of transversely scribed LIG in the composite with 75% PI powders created at the same laser power and speed. With the same laser scribing parameters, the sheet resistance of the as-fabricated longitudinal LIG decreases from 7.5 to 0.175 kΩ □$^{-1}$ as the PI powders increase from 25% to 75% (Figure 2f). However, the resistance of LIG@PI/PDMS/PEIE shows less dependence on laser scribing directions compared to that of LIG@PI.[16] The as-fabricated LIG@PI/PDMS/PEIE with transverse laser scribing shows a much smaller response to stretching up to 12% than the one with longitudinal scribing for the PI$_{0.5}$/PDMS sample (Figure 2g), which is consistent with previous reports.[16] Cyclic tests over 1000 times also reveal the stable electromechanical properties of the LIG@PI/PDMS/PEIE (Figure S6, Supporting Information). The overall stretchability of LIG@PI/PDMS/PEIE can be further increased when combined with stretchable designs such as serpentine, wavy, or kirigami structures.[17] It is worth noting that 12% is sufficient for most on-body applications except for locations with extreme deformations such as joints.[18] The minimum linewidth obtained by CO$_2$ laser scribing is around 150 µm, but a higher resolution can be obtained by green, UV, or femtosecond lasers.[19]

Good hydrophilicity is highly desired for postfunctionalization through dip-coating,[20] in situ reduction,[21] or electroplating[22] to prepare LIG@PI/PDMS/PEIE for various biosensing applications. Before laser scribing, the PI/PDMS/PEIE composite with varying PI contents shows a similar contact angle to the pristine PDMS. The conversion of hydrophobic PDMS to SiC by laser scribing results in a slightly increased contact angle from 109° to 113°, indicating degraded hydrophilicity. However, LIG@PI/PDMS/PEIE provides dramatically improved hydrophilicity, with the contact angle decreased from 51° to 6° as the PI content increases from 25% to 75% (Figure 2h). The large difference in surface wettability between LIG and PI/PDMS/PEIE allows the water drop placed at the interface to be rapidly and efficiently transported to the LIG side. In comparison, LIG@PDMS has a much larger contact angle of ≈100° due to the infiltration of hydrophobic PDMS into the porous LIG (Figure S7, Supporting Information). Meanwhile, PDMS remains highly hydrophobic after laser scribing (Figure S8, Supporting Information), indicating that the improved hydrophilicity of PI/PDMS/PEIE after laser scribing arises from the newly formed LIG. The high hydrophilicity of the LIG@PI/PDM composite with or without PEIE additives can also be maintained during 2 h measurements (Figure 2h; and Figure S9a, Supporting Information) or even over 5 days (Figure S9b, Supporting Information). Overall, increasing the PEIE content can greatly improve the adhesive strength and reduce the modulus of the composite. A high PI content leads to high-quality LIG (i.e., good electrical conductivity and porosity), but at the loss of the composite's mechanical stiffness. As the composite with 75% PI or more corresponds to a low mechanical stiffness, the composite with 50% PI is chosen for high LIG quality and mechanical stiffness in the following investigation unless specified otherwise. The incorporation of PEIE increases the adhesion but at the cost of reduced modulus. As a result, 25 µL PEIE per 10 g PDMS is adopted in the following study.

2.3. Biopotential Monitoring

The strong adhesion and small bending stiffness of the LIG@PI/PDMS/PEIE patch with a thickness of 100 µm allow facile conformal attachment to curvy human skin or tissues without the need for an additional adhesive layer. It is also worth noting that the PET film laminated on the composite also serves as a protection layer from contamination to maintain strong adhesion before use on the skin. The adhesive patch strongly conforms to the human chest and arm, even upon daily movements or severe mechanical deformations such as stretching or squeezing (see **Figure 3a**) due to the good stretchability of the composite. The signal-to-noise ratio (SNR)[23] of 24.7 dB from the measured ECG signals captured by the stretchable adhesive patch is comparable to that (26.4 dB) of gel electrodes (Figure 3b). The excellent adhesive strength of the patch can last for over 24 h. Even after one and two cycles of peeling off and reattaching to the human skin, the adhesive patch was capable of maintaining a high SNR of 23.6 and 23.3 dB in ECG measurement. More importantly, high-fidelity electrophysiological signals, such as ECG and EMG, can be captured in continuous measurements involving artificial deformations. The electrophysiological signal recorded by the LIG@PI/PDMS/PEIE electrodes during the stretching or compression motions (induced with fingers) shows no abnormal deviations in the sinus electrocardiogram waveform, maintaining a high SNR of 22.8 in a 15 s measurement. In contrast, the commercial dry gel electrodes show signal fluctuations during the manually applied skin deformations (black arrow in the

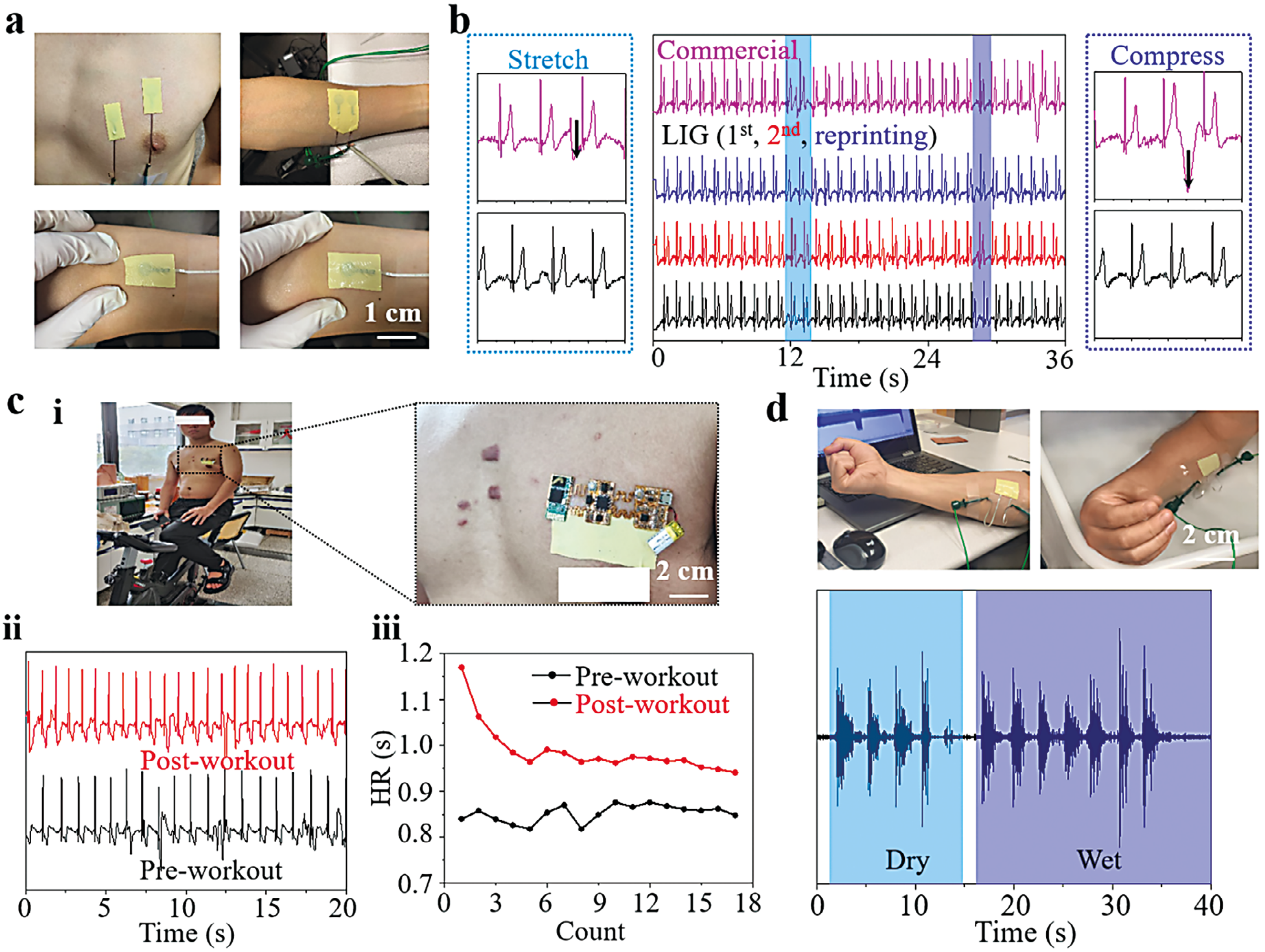

Figure 3. Biopotential measurements by the LIG@PI/PDMS/PEIE-based adhesive patch. a) Optical images of the patch for ECG or EMG measurements upon various deformations. b) Comparison of ECG signals captured by the commercial electrode and the patch during the first and second use, and after reprinting. Artificial deformations were introduced to compare the robustness of various LIG-based bioelectrodes in ECG measurements. The ECG signals under stretching and compression deformations were magnified in the left and right panels, respectively. c, i) Experimental setup of ECG measurements by the LIG@PI/PDMS/PEIE-based adhesive patch with an integrated flexible, miniaturized, wireless data processing unit and built-in Bluetooth module. Measured ii) ECG and iii) extracted heart rate (HR) from ECG of a subject before and after the workout. d) EMG measurements by the LIG@PI/PDMS/PEIE-based adhesive patch in both dry and wet environments.

magnified insets) with a low SNR of 15.5 dB. In comparison, electrodes based on LIG@PI or LIG@PDMS (Figure S10a, Supporting Information) need an additional adhesive to interface with the skin and the measured ECG signals are vulnerable to skin deformations (Figure S10b, Supporting Information). Integrated with a portable, custom-built signal processing system consisting of a 2-channel low-power analog front end and a built-in Bluetooth module (circuit design in Figure S11, Supporting Information), the adhesive patch can provide stable ECG monitoring after indoor workouts (Figure 3c–i) with obvious sweat secretion (Figure 3c–ii). The heat rate (HR) of the human subject elevates from ≈0.85 to ≈1.15 s after running and then recovers to ≈0.9 s during rest after running (Figure 3c–iii).

The hydrophobicity of PI/PDMS/PEIE also allows the composite to be used in wet or aqueous environments. Excellent sealing is achieved by a thin PDMS encapsulation and connecting the LIG electrode on the patch with thin silver stripes through a via filled with liquid metal that also avoids mechanical mismatch at the interface. EMG signals from clenching the fist are captured with high fidelity (SNR of 21.8 or 22.3 dB) in a dry state or submerged in water (Figure 3d; and Video S1, Supporting Information). The short and long clench in the captured EMG signals can be accurately distinguished (Figure S12, Supporting Information). No signs of skin rashes are observed after 24 h of wearing on the arm, indicating good biocompatibility and gas permeability of the patch (Figure S13, Supporting Information). The adhesive patch is also reprogrammable and reusable, which can be simply achieved by peeling off the LIG pattern with scotch tape followed by a laser rewriting process (Figure S14, Supporting Information). The patch is thinned down by ≈20 µm after each laser scribing cycle and the one with an initial thickness of 100 µm can be rewritten for ≈3–4 times. The adhesive patch not only maintains a high SNR of 23.8 dB after three rewriting processes in the measured ECG but also exhibits more robust

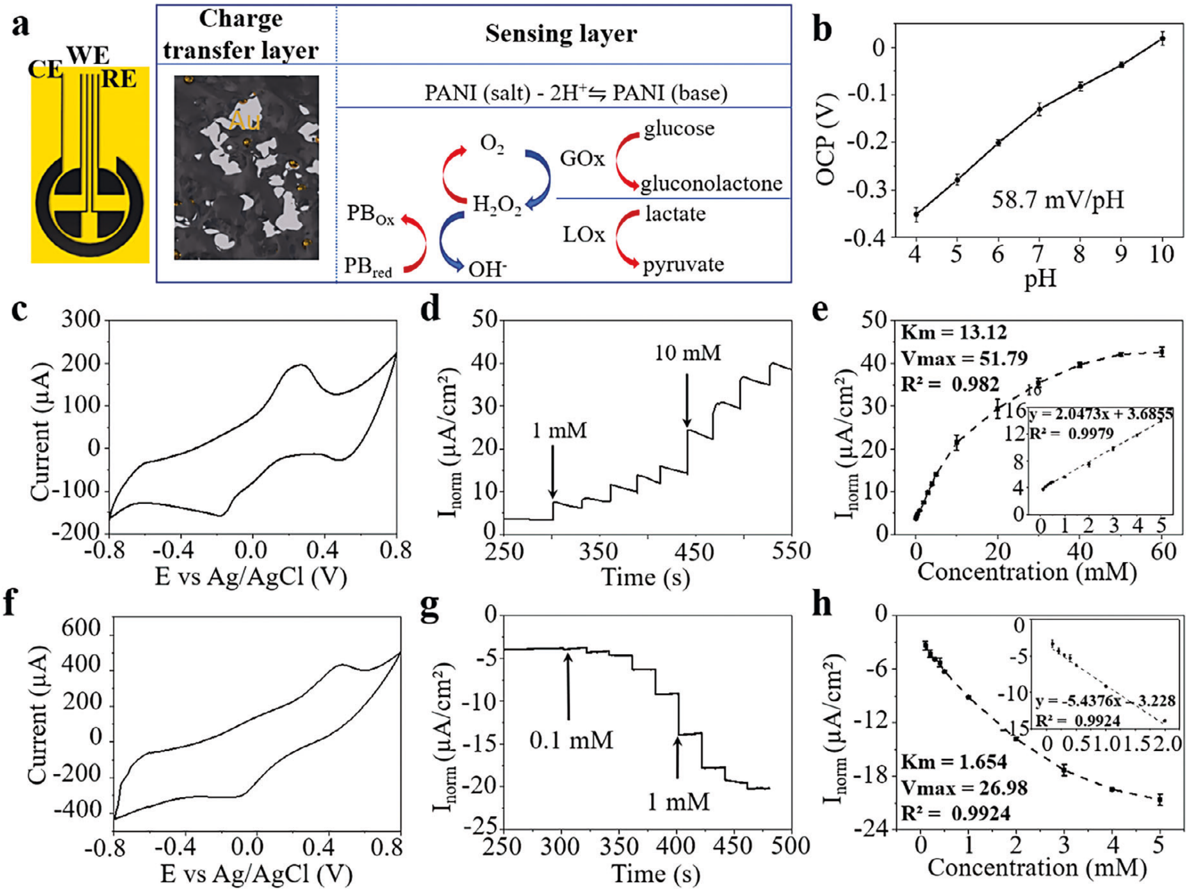

Figure 4. Characterization of the LIG@PI/PDMS/PEIE-based electrochemical sensors toward pH, glucose, and lactate. a) Schematic of the electrochemical sensing mechanism. b) Open-circuit potential (OCP) of the PANI/AuNP/LIG-based electrode versus an Ag/AgCl quasi-reference electrode. c) CV curve of the GOx/PB/AuNP/LIG electrode in 0.2 м PBS (pH 6.5) in the presence of 1 mм glucose with a scan rate of 50 mV s^{-1}. d) Amperometry response of the working electrode to consecutive injection of glucose into the stirred 0.2 м PBS (pH 6.5) with an applied potential of 0.26 V (i.e., the oxidation peak) and e) corresponding data fitted to the Michaelis–Menten equation by using nonlinear regression analysis for GOx and the corresponding calibration curve. f) CV curve of the LOx/PB/AuNP/LIG electrode in 0.2 м PBS (pH 6.5) in the presence of 1 mм lactate with scan rate 50 mV s^{-1}. g) Amperometry response of the working electrode to consecutive injection of lactate into the stirred 0.2 м PBS (pH 6.5) with an applied potential of −0.1 V (i.e., the reduction peak) and h) the corresponding calibration curve.

mechanical properties against deformation, which can be attributed to reduced thickness and mechanical stiffness (Figure S15a, Supporting Information). Similarly, EMG signals can be captured by the rewritten patch in both dry and wet environments (Figure S15b, Supporting Information).

2.4. Electrochemical Sensing of pH, Glucose, and Lactate

Combined with simple functionalization (e.g., drop casting,[20] electrodeposition,[24] electroless plating,[4,12c] or adding additives in carbon precursors),[5,25] the LIG with the porous structure and large specific surface area can be leveraged for energy storage and chemical/electrochemical biosensing. The importance of good hydrophilicity is revealed by depositing Prussian Blue (PB) on LIG@PI/PDMS/PEIE and LIG@PDMS with the cyclic voltammetry (CV) technique at a bias window from 0 to 1.0 V (Figure S16, Supporting Information). The hydrophilic LIG@PI/PDMS/PEIE with high porosity despite high resistance still exhibits a much higher current than the negligible value of LIG@PDMS, indicating the high efficiency of chemical modifications by electroplating. Compared with LIG@PDMS with reduced porosity and hydrophilicity, LIG@PI/PDMS/PEIE could provide a multifunctional bioadhesive patch for multiplexed electrochemical sensing of various biomarkers, such as pH, glucose, and lactic acid (**Figure 4**a). The fabrication of the electrochemical sensors starts with electroplating Au nanoparticles (AuNPs) on the LIG working electrode (WE) to improve the charge transfer efficiency, which is similar to spray-coating AgNWs on LIG as in the literature.[6] The AuNP-modified LIG WE modified by electroplated polyaniline (PANI) is then combined with an Ag/AgCl reference electrode in a two-electrode configuration to measure pH. Because the reaction potential of PANI depends on the proton concentration or the pH value, the measured open circuit potential (OCP) changes linearly with the pH value, with a sensitivity of 58.7 mV pH^{-1} (close to the Nernst limit) calculated from the slope of the linear fitting curve (Figure 4b). The LIG@PI/PDMS/PEIE-based patch not only shows comparable pH sensing performance to that of the previously reported LIG@PI-based one[26] but also owns intrinsic stretchability and adhesion for improved practicality of skin-interfaced electronics.

The immobilization of biorecognition elements or specific receptor molecules such as enzymes, aptamers, or antibodies on the LIG electrodes can also prepare electrochemical sensors for selective and sensitive detection of target analytes in biological samples. In a proof-of-the-concept demonstration to detect glucose and lactate, a thin layer of Prussian blue (PB) and gold nanoparticles (AuNPs) is first in situ co-electrodeposited on LIG using cyclic voltammetry to help immobilize enzymes due to its high surface area, stability, and biocompatibility.[27] The favorable electrochemical properties (high electron conductivity and redox behavior) with efficient signal transduction and amplification can also increase selectivity and stability.[28] The biomarker radicals or hydrogen peroxide produced after interacting biomarkers with the enzyme would oxidize or reduce Prussian blue to generate an electrical signal that can be measured and correlated to the biomarker concentration (Figure 4a). Further immobilizing the electrode with enzymes such as GOx and LOx in the WE provides the resulting electrochemical sensor in a three-electrode configuration to detect glucose (Figure 4c–e) and lactate (Figure 4f–h). The cyclic voltammetry (CV) tests of the glucose and lactate biosensor are measured between −0.8 and 0.8 V at a scan rate of 50 mV s^{-1} in 0.2 M PBS (pH 6.5) solution with 1 M glucose and lactate, respectively (Figure 4c,f). A bias potential of 0.26 V (vs Ag/AgCl) for glucose and −0.1 V for lactate was employed to avoid interferences. The amperometric detection of consecutively injected glucose under stirring with the PB-GOx-modified LIG electrode at 0.26 V shows a linear dependence of the measured current ΔI (μA cm^{-2}) on the glucose concentration from 100 μM to 5 mM, with a slope or sensitivity of 2.0473 μA cm^{-2} mM^{-1} and a correlation coefficient of 0.9927 (Figure 4d). Similarly, the PB-LOx-modified LIG electrode at −0.1 V detects the consecutively injected lactate from 100 μM to 2 mM with a sensitivity of 5.4376 μA cm^{-2} mM^{-1} and correlation coefficient of 0.9924 according to ΔI (μA cm^{-2}) = −3.228–5.4376 [lactate] (mM) (Figure 4g). The use of the Michaelis–Menten equation (39)[29] further reveals the kinetic behavior of the lactate and glucose sensor. This behavior analysis of the glucose and lactate oxidase enzymes allows the determination of kinetic parameters for further performance optimization of the enzymatic electrochemical sensors. The apparent Michaelis–Menten constant (K_m) and the maximum steady-state current response (I_{max}) are determined to be 13.12 mM and 51.79 μA cm^{-2} ($n = 3$) for glucose concentrations from 100 μM to 60 mM (or 1.654 mM and 26.98 μA cm^{-2} for lactate from 100 μM to 5 mM). Those determined values for glucose and lactate sensors represent the great ability of the sensor to produce an electrical signal in response to a high concentration of glucose or lactate with good sensitivity to detect lower glucose or lactate concentrations in the sweat. The linear working range and sensitivity of the LIG@PI/PDMS/PEIE-based electrochemical sensor are significantly larger than those based on LIG@PDMS[6] thanks to the well-preserved porosity for enzyme loading. A comparison of sensitivity, limit of detection (LOD), and working range to other transferred LIG-based (LIG@PDMS) electrochemical sensors (not limited to glucose)[6,30] was given in Table S2 (Supporting Information).

2.5. Enhanced Conductivity for DC Interconnects and RF Devices

Different from the resistive sensing unit in favor of higher resistance for precise measurements (e.g., strain/temperature sensing),[9b] the other functional components (e.g., wiring/interconnects, electrodes, heaters, or RF units) are supposed to have high conductivity. To obviate the need for radically different materials and fabrication processes, it is highly desirable to exploit and fabricate conductive LIG@PI/PDMS/PEIE patterns with spatial-dependent conductivity to avoid mechanical mismatch at the interface for improved durability and long-term use. Besides the ease of integration with circuit boards over "fly-over" wires, the minimized mechanical mismatch at the hetero-integrated interface could also avoid electrical failure under deformations. Due to the high hydrophilicity and porosity, the LIG in the composite can be selectively modified with highly conductive dopants, such as drop-casting of silver nanoparticle (AgNP) ink, electrodeless plating of nickel, or air-spraying of silver nanowires (AgNWs) (**Figure 5**a). The sheet resistance of the modified LIG with nickel, AgNPs, and AgNWs reduces to 1.3, 3.1, and 5.6 $\Omega\ \square^{-1}$. The porosity of LIG decreases with the introduction of Ni or AgNPs but was well maintained with the modification of AgNWs because of the larger dimension of AgNWs than the pore size (Figure S17, Supporting Information).

Electroless plating of Ni on LIG with winding structures results in a flexible heater that can rapidly heat up from 24 °C (i.e., the room temperature) to 105 °C as the applied bias voltage increases from 0 to 12 V (Figure 5b). The relatively uniform temperature distribution in the heater confirms the uniform coating by electroless plating to improve the conductivity. RF devices are also in favor of high conductivity due to reduced ohm loss. As a result, drop-casting AgNP ink on LIG followed by photonic sintering reduces the sheet resistance from 5241 to 3.1 $\Omega\ \square^{-1}$, promising common RF devices, such as wideband dipole antennas and near-field communication (NFC) coils. The flexible wideband dipole antenna based on AgNP/LIG shows characteristic "dual-resonance" and a low reflection coefficient ($S_{11} < -10$ dB) at resonant frequencies (Figure 5c), whereas the one based on pristine LIG does not show observable resonance due to its large electrical resistance. The dual resonance and low reflection of the AgNP/LIG-based dipole antenna contribute to a wide operational bandwidth (>0.4 GHz), which also remains unchanged upon bending deformations for potential applications in on-body wireless communication and RF energy harvesting.[31] Simulations reveal the typical dipole-like impedance curves and radiation patterns (Figure S18a–c, Supporting Information). Five antennas fabricated by the same procedure only exhibit a relatively small resistance variation of <10% and similar S_{11} curves (Figure S18d, Supporting Information), resulting in a variation of <3% for the radiation efficiency. An NFC coil with a designed inductance of ≈5 nH can be combined in series with a commercial NFC chip with an internal capacitance of 27.5 pF to resonate at ≈13.56 MHz for near-field communication with smartphones (Figure 5d). The AgNP/LIG-based coil exhibits a modest Q factor of ≈15.2 at 13.56 MHz (Figure S19, Supporting Information) with a broad frequency response for robust performance upon bending deformations.[32] According to the min-phase method,[33] the resonant frequency of the LC circuit can be determined by the inflection point of the reflection curve

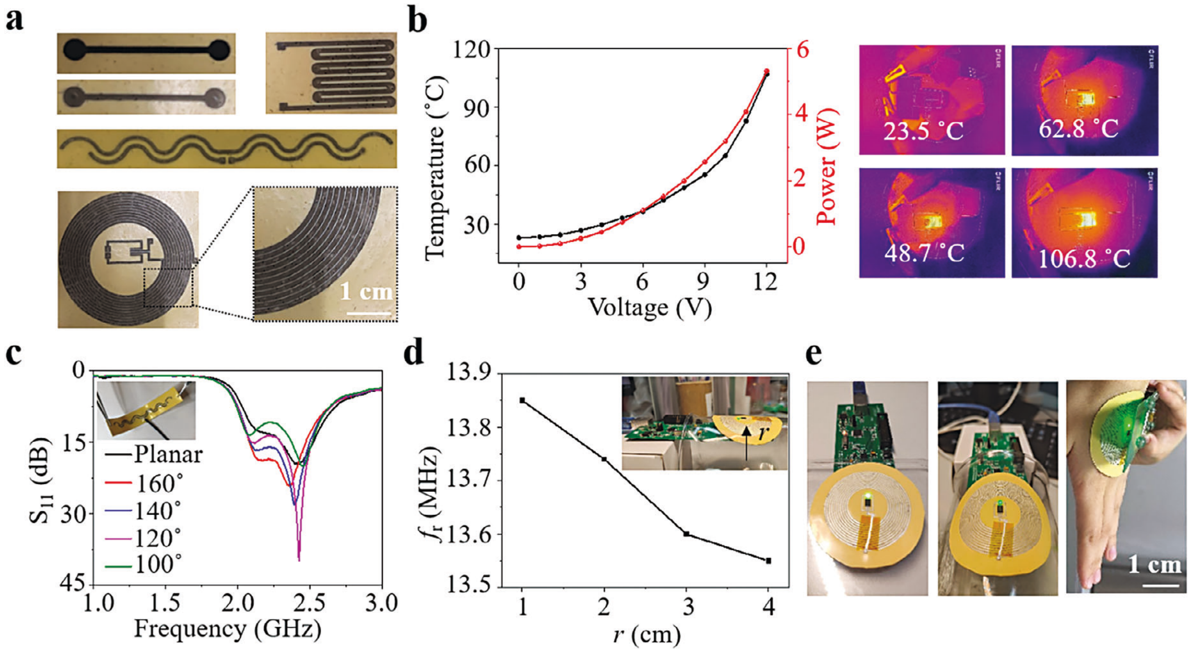

Figure 5. Metallic modifications on LIG for improved conductivity to enable DC/AC applications. a) Optical images of the LIG electrode modified by electroless plating of nickel (top), air-spraying of silver nanowires (AgNWs) (middle), and drop-casting of Ag nanoparticle (AgNP) ink (bottom). b) Heating performance of the Ni/LIG-based flexible heater. c) S_{11} curves of a wideband AgNW/LIG-based dipole antenna with double-arm configurations under bending deformations. d) Resonant frequency of an AgNW/LIG-based NFC device under bending deformations determined by the "Min-phase" method. e) Optical image of the NFC device wirelessly powered by a transmitter to light an LED.

(Figure S20, Supporting Information). The negligible difference between the measured (13.56 MHz) and simulated (13.55 MHz) resonant frequency indicates excellent manufacturability of the approach. For a bending radius of 1 cm, the resonant frequency only slightly shifts from 13.55 to 13.84 MHz, allowing for robust wireless communication and powering (Figure 5d, e). To summarize, laser scribing exhibits the advantages of high precision, low cost, and scalable production in antenna fabrication.

2.6. Multifunctional Skin-Interfaced Platform Based on LIG@PI/PDMS/PEIE

Spatial-dependent modifications on the stretchable adhesive LIG@PI/PDMS/PEIE patch afford a wirelessly powered drug delivery system for wound healing. After immobilizing Cefazolin antibiotics on LIG electrodes with the assistance of polypyrrole (PPy) by electroplating,[34] applying negative bias releases the negatively charged Cefazolin molecules, with PPy changed from the oxidized to reduced state. The efficacy of the controllable drug release is first evaluated by using fluorescein as a model drug molecule in preliminary experiments. Applying a positive bias of −1.5 V for 5 min changes the transparent electrolyte to green, indicating the effectiveness of electrically controlled fluorescein release (**Figure** 6a–i). The Cefazolin-modified LIG electrode is then combined with the aforementioned AgNP/LIG-based NFC coil for wirelessly controlled drug delivery (Figure 6a–ii). Despite the modest Q factor, the coil ensures combined with the NFC chip can still generate an output voltage of 1.5 V after built-in rectification to power a UV LED and simultaneously trigger drug delivery. AgNP/LIG-based NFC devices include one with drug-loaded electrodes and LED (I), one with drug-loaded electrodes (II) or LED (III), and another blank one as the control (IV) (Figure 6a–iii). Evaluation of the antibacterial effect of these four AgNP/LIG-based NFC devices relies on the zone of inhibition (ZOI). The harvested energy from an RF transmitter is applied between the work and counter electrodes to trigger drug delivery. In all cases, the wireless stimulation duration is set to 1 h, and optical images of bacteria colonies and corresponding ZOI defined as the width of the bacteriostatic ring (w) are collected after 24 h culture in an incubator. Also, different working distances (i.e., 1 and 22 mm) between the device and transmitter for Group I are tested to investigate its influence on drug delivery. The output voltage of the coil after rectification and splitting remains ≈1.5 V with an increasing distance up to 19 mm, and then drops to ≈0.2 V at 20 mm (Figure 6a–iv). A zero ZOI in Groups III and IV indicates the inefficacy of bare electrical stimulation or LED illumination against *S. aureus*. In comparison, Group I shows a significantly larger ZOI, which is almost close to that of Group II (Figure 6a–v), indicating effective antibiotic delivery through wirelessly controlled stimulation. However, increasing the working distance to 20 mm in Group I (i.e., I@20 mm) decreases the ZOI to ≈0.3 mm due to reduced bias. Although UV LED does not directly inhibit *S. aureus*, it can serve as an indicator of the working distance to ensure effective drug delivery. Besides, it is possible to incorporate light-responsive hydrogels or photothermal effects to further boost the antibacterial performance.[35] Considering the good adhesion, antibacterial capability, and possibly the electrical stimulation and photothermal effect, the

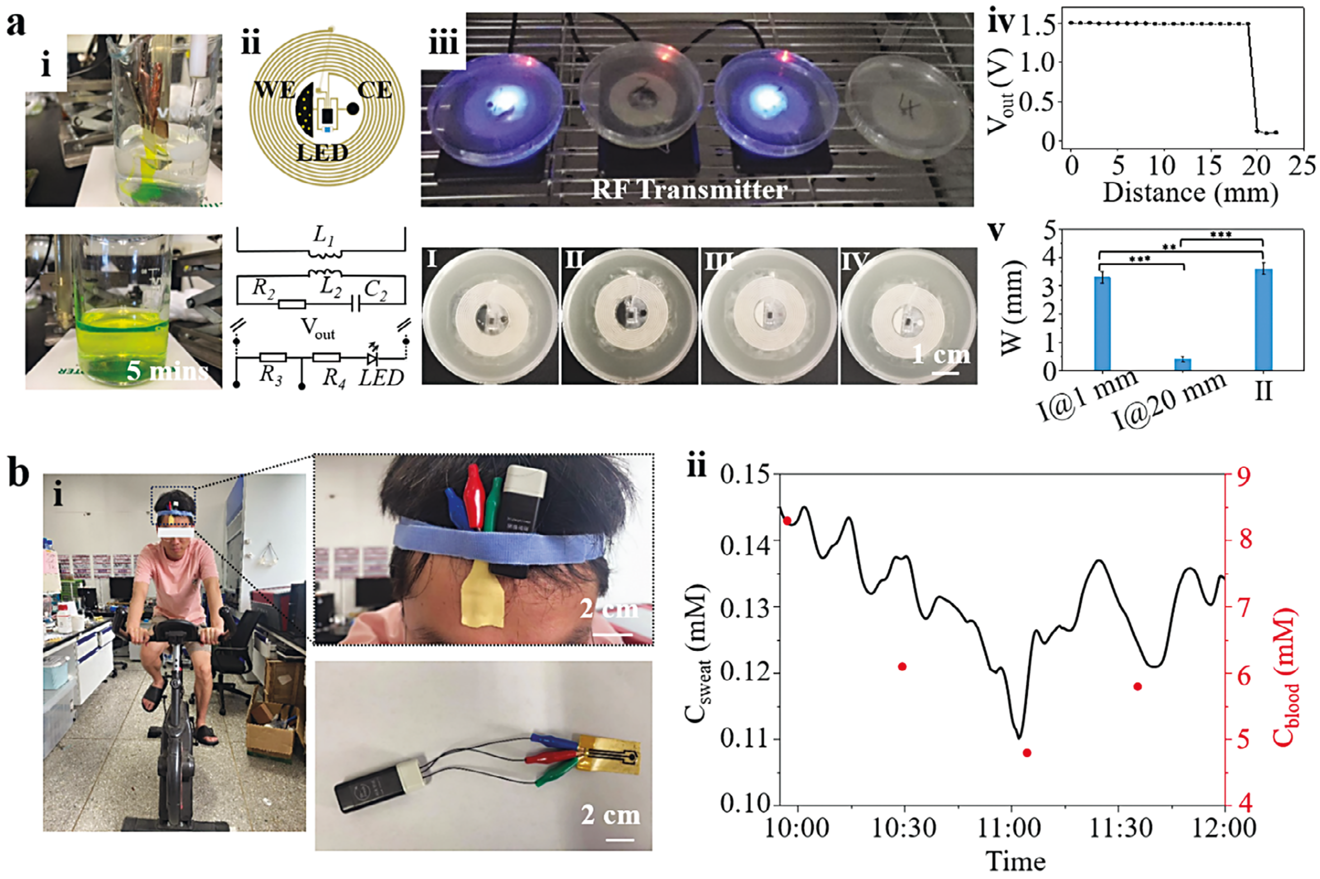

Figure 6. Multifunctional skin-interfaced platform based on LIG@PI/PDMS/PEIE. a) Wirelessly controlled drug delivery system based on the LIG@PI/PDMS/PEIE for antibacterial wound healing. i) Optical images of the fluorescein release upon an applied voltage of −1.5 V. ii) Schematic of the drug delivery device and the corresponding circuit model. iii) Optical images of the dual-functional LIG@PI/PDMS/PEIE-based patch with wirelessly controlled drug delivery and UV-LED indicator. iv) Output voltage (V_{out}) as a function of the distance between the device and transmitter. v) Antibacterial performance of dual-functional LIG@PI/PDMS/PEIE patch ($^{*}p < 0.05$; $^{**}p < 0.01$; $^{***}p < 0.001$). b) Skin-interfacing real-time sweat glucose sensing patch based on LIG@PI/PDMS/PEIE. i) Optical images of the sweat glucose sensing patch and experimental setup for real-time measurements. ii) Real-time sweat (C_{sweat}) and blood (C_{blood}) glucose concentration during in-door workouts measured by the patch and commercial finger prick blood test, respectively.

AgNP/LIG-based adhesive device platform holds great potential in wound healing.

The system-level demonstration is showcased by integrating the adhesive LIG@PI/PDMS/PEIE patch with a miniaturized and portable electrochemical station on the forehead with a headband for real-time sweat glucose sensing (Figure 6b-i). The extended interconnects between the glucose sensor and the electrochemical station exploit LIG/AgNWs for reduced electrical resistance. The large difference in hydrophilicity between LIG and PI/PDMS/PEIE allows efficient sampling and transport of the sweat to the LIG-based glucose sensor, without the need for a microfluidic module. The sweat glucose concentration of a subject is continuously measured for 2 h during in-door bicycling. The measured results show the elevated sweat glucose concentration (≈0.145 mM) 1 h later after having breakfast at 9:00 am (Figure 6b-ii). With continuous workouts, the sweat glucose concentration slowly drops to ≈0.11 mM at 11:00 am due to the large consumption of calories.[36] However, a slight increase in sweat glucose concentration is observed after that, possibly attributed to the glycogenolysis or gluconeogenesis process.[37] The sweat glucose concentration is also compared with the blood glucose concentration measured with a commercial glucose sensor by finger pricking every 30 min between 9:30 and 11:30 am. The trend of increasing after breakfast and dropping during a workout followed by a slight increase afterward in the blood glucose concentration correlates well with the continuously measured sweat glucose concentration, with a delay of 30 min. This delay is believed to arise from the diffusion process of glucose from blood to interstitial fluid and sweat.[38] It may be possible to directly obtain accurate blood glucose concentration by accounting for this time delay and other sweat parameters, such as pH and perspiration rate to help calibrate the measurements.[39]

3. Conclusion

In this work, we introduced an on-demand, programmable, recyclable device platform based on PI/PDMS composites for multifunctional, skin-interfaced applications. The incorporation of PI and PEIE enables laser processing of the composite for electrical or sensing functionalization and strong adhesion for direct skin-interfacing. LIG fabricated on the PI/PDMS composite allows high-fidelity biopotential measurements of a subject during workouts or in a wet-skin state. Postmodifications of porous LIG on the adhesive composite with functional materials contribute to electrochemical sensing of bio-relevant parameters of sweat, including the pH value, glucose, and lactate concentration. Spatial-dependent modifications of LIG toward electrical and sensing functions were capable of realizing simple device-level integrations on the same material platform (i.e., LIG@PI/PDMS/PEIE). Successful real-time monitoring of ECG, EMG, and sweat glucose concentration based on the LIG@PI/PDMS/PEIE-based sensing platform has been demonstrated. This material design strategy is also applicable to other polymers, such as thermoplastic polyurethane (TPU) or styrene-ethylene-butylene-styrene (SEBS), resulting in functional composites with different mechanical and electrical properties for broad application scenarios (Figure S21, Supporting Information).

4. Experimental Section

Fabrication of LIG@ PI/PDMS/PEIE: The fabrication of elastomeric bioadhesives started with manual mixing of PDMS (Sylgard 184), PI power (Evonik, P84 NT, 6 µm), and PEIE with varying mass ratios. A mass mixing ratio of 1:0.25, 1:0.5, and 1:0.75 of PDMS to PI power was studied. The PEIE was added to the mixture to reduce the crosslinking of PDMS for improved adhesion of the resulting composite. The PDMS/PI/PEIE mixture diluted by heptane was spin-coated on a silicon wafer treated with a sacrificial PVA layer. After spin coating for 60 s at a speed of 500 rpm, the wafer was transferred to an oven at 80 °C for 1 h. Increasing the curing time resulted in decreased adhesion and increased stiffness. A thin PET film of 20 µm was attached to the cured composite to avoid potential contamination and maintain the adhesion of the composite in the following processes. A CO_2 laser with a wavelength of 10.6 µm and a spot size of ≈130 µm was used to first cut the PET film in the vector mode to expose the underlying composite and then created LIG patterns in the raster mode (power of 10.5%, speed of 11%, PPI of 1000, and image density of 6). Peeling the resulting film off from the silicon wafer created porous LIG in PDMS/PEIE. The remaining PET would serve as a mask in the following steps. Gentle air flow was employed to remove the LIG debris before chemical modifications or measurements.

Biopotential Measurements with the LIG@PI/PDMS/PEIE: After wiring with silver pastes, the LIG@PI/PDMS/PEIE adhesive patch was applied to the clean skin treated with alcohol wipes. A multichannel data acquisition system (PowerLab 16/35) combined with an amplifier (Bio Amp) was used to measure ECG and EMG at a sampling rate of 1000 Hz. An analog/hardware bandpass filter (10–200 Hz) implemented in Bio Amp was applied before the A/D conversion for the raw ECG and EMG sampling. The small baseline drift in the raw ECG/EMG data indicated effective suppression of both the thermal noise and Flicker noise. The SNR of raw EMG signals was calculated as the ratio of the root-mean-square value of the raw EMG signal during muscle contraction to that at rest. The power spectral density of raw ECG and EMG signals was obtained by using Welch's method implemented in MATLAB with a fast Fourier transform (FFT) size of 1000% and 50% window overlap (Figure S22, Supporting Information). The high-pass digital filters were not applied to remove Flicker noise from the raw data due to its strong coupling with the signal in the low-frequency range. The SNR of ECG signals was calculated as the ratio of the power in the frequency range of interest (0–100 Hz) to that in the high-frequency range (i.e., the thermal noise). The SNR induced by the motion artifacts was calculated by following the method reported previously.[23] In brief, the noise induced by the motion artifacts was first obtained by applying a low-pass filter (1 Hz). The ECG and EMG signals were obtained by subtracting the noise from the raw data. The SNR corresponding to motion artifacts was calculated as the ratio of the root-mean-square value of the signal after subtracting the noise to that of the noise.

Fabrication of LIG-Based REs: A drop of AgNP ink was added to the as-fabricated composite electrode, followed by annealing in an oven at 80 °C for 10 min. Next, the electrode was immersed in a $FeCl_3$ solution for 1 min for colorizations and then rinsed with DI water. After drying in air, 20 µL PVB cocktail solution (79.1 mg of PVB, 50 mg of NaCl, 1 mg of F127, and 0.2 mg of multiwalled CNT in 1 mL of methanol) was drop-cast on the electrode. Afterward, 10 µL diluted Nafion solution was coated on the PVB-modified electrode to complete the fabrication of LIG-based RE.

Fabrication of LIG-Based WEs for pH and Glucose/Lactate Sensing: For pH sensing, the obtained electrode was then modified by electroplating PANI. After mixing 0.1 м aniline and 1 м H_2SO_4 to prepare the electroplating solution, CV deposition of PANI from −0.2 to 1 V with respect to a commercial Ag/AgCl reference electrode was performed at a scan rate of 0.05 V s^{-1} for 30 cycles, followed by rinsing with DI water. The characterization of PANI was carried out by CV in 1 м HCl with a scan rate of 0.1 V s^{-1}. pH measurements were carried out by combining the WE and LIG-based RE in a two-electrode system.

The fabrication of the WE was conducted under the in situ electrodeposition of PB and AuNPs. The electrodeposition was performed by cyclic voltammetry (CV) between −0.2 and 0.8 V (vs Ag/AgCl) at a scan rate of 0.1 V s^{-1} for 90 cycles in a freshly prepared mixed solution of 250 mg L^{-1} $HAuCl_4$, 2×10^{-3} м $FeCl_3$, 2×10^{-3} м $K_3[Fe(CN)_6]$, 0.1 м KCl, 0.01 м HCl, and DI water. After electrodeposition, the as-fabricated WE was rinsed with DI water and dried in ambient conditions. Then, the PB/AuNP/LIG electrode was modified by GOx (concentration of 34 mg mL^{-1} in DI water) mixed with the chitosan solution at a 1:1 wt% ratio. The chitosan solution was prepared by mixing 2 wt% chitosan and 2 wt% acetic acid solution with an additional 0.8 wt% glycerol in DI water at 80 °C. Similarly, mixing the obtained chitosan solution with LOx (34 mg mL^{-1} in DI water) at a 1:1 wt% ratio prepared the LOx solution. The completed LOx solution was stored at −10 °C for future use after complete mixing. After drop-casting the prepared LOx solution on the PB/AuNP/LIG WE and drying in the ambient condition, 5 wt% glutaraldehyde and 1 wt% Nafion were drop-casted. The resulting WE for lactate sensing was stored at 4 °C overnight before testing.

Fabrication of LIG Composite-Based Wiring and Interconnects: Metallic nanomaterials (AgNWs, Ni, and AgNPs ink) were prepared on the LIG composite (with PET as a self-mask to define the patterns) to improve its conductivity for electrical interconnects or RF applications. Diluted AgNWs (AgNWs-60, ACS material) solution by isopropyl alcohol (IPA) with a ratio of 1/10 v/v was sprayed on the LIG composite by a commercial airbrush (G222; Master Airbrush), with the nozzle fixed at a distance of 20 cm from the substrate and an airbrush pressure of ≈20 psi. The PET self-mask was removed after the evaporation of IPA. The Ni layer was deposited on the LIG composite through electroless plating, using commercial electroless plating precursor solutions. In brief, after surface activation of the LIG composite by pretreating with A, B, and C solutions in sequence, immersing in D solution at 65 °C for 30 s completed the electroless plating process. AgNP inks (JS-A911, Novacentix) were manually air-sprayed on the LIG composite. After the solvent evaporation, annealing with a xenon light through photosintering (Xenon Corporation, X-1100) for three pulses (pulse duration of 529 µs, energy of 1000 J, and voltage of 3000 V) yielded a conductive Ag coating on the LIG composite.

Materials Characterization: The Raman spectrum was measured by Horiba (HORIBA, Ltd.) with a 532 nm laser source. SEM characterization of LIG was carried out with TESCAN MIRA3 (TESCAN ORSAY HOLDING). Mechanical stiffness and adhesion measurements were carried out with a universal testing machine (M230Pro, Hengyi Precision Instruments Limited Company), with the stretching and peeling-off rate set to 10 and 200 mm min^{-1}, respectively. The electromechanical properties of the LIG@PI/PDMS/PIEI were carried out by stepwise stretching with a custom-built stretching system and a sourcemeter (Keysight 2902). Fatigue tests were performed by cyclic stretching at a rate of 0.5% s^{-1}.

Modification of LIG Electrodes for Drug Delivery: Polypyrrole (PPy) modifications on LIG electrodes for drug delivery were achieved by electropolymerization of pyrrole monomers in a three-electrode configuration with a commercial Ag/AgCl reference electrode and a Pt counter electrode. A constant current of 0.1 mA cm^{-2} was applied to LIG in a solution containing 0.1 м pyrrole and 0.01 м cefazolin sodium for 360 s. Next, cefazolin antibiotics were loaded as dopants in PPy by electrodeposition at a constant current density of 0.5 mA cm^{-2} in a solution for 360 s with 0.1 м pyrrole and 0.01 м cefazolin sodium. Afterward, another layer of PPy was electropolymerized as encapsulations with the same setup. The obtained electrode was then rinsed with DI water. The PPy/fluorescein layer was electrodeposited with the same procedure except that 0.01 м cefazolin sodium was replaced by 0.1 м fluorescein. The obtained working electrode was combined with a bare LIG counter and reference electrodes in a three-electrode configuration.

Antibacterial Tests: Four devices (i.e., Group I, II, III, and IV) were first treated by alcohol and UV sterilization before being attached to the bottom of Petri dishes for bacterial culture. Agar was uniformly applied on the device for grafting of bacterial suspension, followed by bacterial culture in the incubator. A wireless transmitter was placed under the petri dish in Groups I, II, and III to trigger the LED illumination and/or drug release for 1 h. After a 24 h culture, the antimicrobial activity was evaluated by measuring the area of ZOI.

On-Body Tests: Before the application of the adhesive LIG@PI/PDMS/PEIE patch for sweat glucose sensing, the forehead skin of the subject was cleaned with alcohol wipes. Then, the adhesive patch was wired with a miniaturized, wireless electrochemical station (BioSYS-P15E Max, Shenzhen Refresh Biosensing Technology Co., Ltd). Afterward, the subject was required to do indoor cycling for sweat sampling and glucose measurements. All human subject studies were approved by the Institutional Review Board at Penn State University (#STUDY00020934).

Supporting Information

Supporting Information is available from the Wiley Online Library or from the author.

Acknowledgements

This work was supported by the Natural Science Foundation of China under Grant Nos. U21A20460, 62301116, 52021001, and 61825102, and the Medico-Engineering Cooperation Funds, Fundamental Research Funds for the Central Universities, UESTC under Grant No. ZYGX2021YGLH002. H.C. acknowledged the support provided by NIH (Award No. R21EB030140), NSF (Grant Nos. 2309323, 2243979, 2319139, and 2222654), and Penn State University. The authors would like to thank Mr. Robert Lavalle and Mr. Daniel Erdely at Penn State for their help in SEM characterization.

Conflict of Interest

The authors declare no conflict of interest.

Data Availability Statement

The data that support the findings of this study are available from the corresponding author upon reasonable request.

Keywords

bioadhesive, electrochemical sensors, laser fabrication, recyclable electronics, skin-interfaced devices

Received: January 5, 2024
Revised: March 26, 2024
Published online:

[1] a) W. Gao, H. Ota, D. Kiriya, K. Takei, A. Javey, *Acc. Chem. Res.* **2019**, *52*, 523; b) Y. R. Yang, Y. Song, X. J. Bo, J. H. Min, O. S. Pak, L. L. Zhu, M. Q. Wang, J. B. Tu, A. Kogan, H. X. Zhang, T. K. Hsiai, Z. P. Li, W. Gao, *Nat. Biotechnol.* **2020**, *38*, 217; c) M. Q. Wang, Y. R. Yang, J. H. Min, Y. Song, J. B. Tu, D. Mukasa, C. Ye, C. H. Xu, N. Heflin, J. S. McCune, T. K. Hsiai, Z. P. Li, W. Gao, *Nat. Biomed. Eng.* **2022**, *6*, 1225; d) R. M. Torrente-Rodríguez, H. Lukas, J. B. Tu, J. H. Min, Y. R. Yang, C. H. Xu, H. B. Rossiter, W. Gao, *Matter* **2020**, *3*, 1981.
[2] Z. Y. Hui, L. R. Zhang, G. Z. Ren, G. Z. Sun, H. D. Yu, W. Huang, *Adv. Mater.* **2023**, *35*, 29.
[3] a) H. Yoon, J. Nah, H. Kim, S. Ko, M. Sharifuzzaman, S. C. Barman, X. Xuan, J. Kim, J. Y. Park, *Sens. Actuators, B* **2020**, *311*, 127866; b) J. Zhao, N. Yi, X. H. Ding, S. B. Liu, J. Zhu, A. C. Castonguay, Y. Y. Gao, L. D. Zarzar, H. Y. Cheng, *Chem. Eng. J.* **2023**, *456*, 140956.
[4] J. Zhu, S. B. Liu, Z. H. Hu, X. Z. Zhang, N. Yi, K. R. Tang, M. G. Dexheimer, X. J. Lian, Q. Wang, J. Yang, J. Gray, H. Y. Cheng, *Biosens. Bioelectron.* **2021**, *193*, 113606.
[5] Z. W. Peng, R. Q. Ye, J. A. Mann, D. Zakhidov, Y. L. Li, P. R. Smalley, J. Lin, J. M. Tour, *ACS Nano* **2015**, *9*, 5868.
[6] X. Xuan, J. Y. Kim, X. Hui, P. S. Das, H. S. Yoon, J. Y. Park, *Biosens. Bioelectron.* **2018**, *120*, 160.
[7] a) Y. F. Rao, M. Yuan, F. Luo, H. Li, J. B. Yu, X. P. Chen, *J. Colloid Interface Sci.* **2022**, *610*, 775; b) P. Zaccagnini, C. Ballin, M. Fontana, M. Parmeggiani, S. Bianco, S. Stassi, A. Pedico, S. Ferrero, A. Lamberti, *Adv. Mater. Interfaces* **2021**, *8*, 2101046.
[8] Y. Jiang, S. B. Ji, J. Sun, J. P. Huang, Y. H. Li, G. J. Zou, T. Salim, C. X. Wang, W. L. Li, H. R. Jin, J. Xu, S. H. Wang, T. Lei, X. Z. Yan, W. Y. X. Peh, S. C. Yen, Z. H. Liu, M. Yu, H. Zhao, Z. C. Lu, G. L. Li, H. J. Gao, Z. Y. Liu, Z. A. Bao, X. D. Chen, *Nature* **2023**, *614*, 456.
[9] a) C. Zhang, X. H. Ding, H. Y. Cheng, J. G. Chen, J. D. Gao, G. L. Tan, S. B. Bai, K. W. Weng, H. M. Chen, Y. H. Yang, J. Wang, *Nano Lett.* **2023**, *23*, 3435; b) S. Gong, L. W. Yap, Y. Zhu, B. W. Zhu, Y. Wang, Y. Z. Ling, Y. M. Zhao, T. C. An, Y. R. Lu, W. L. Cheng, *Adv. Funct. Mater.* **2020**, *30*, 1910717; c) D. Jung, C. Lim, C. Park, Y. Kim, M. Kim, S. Lee, H. Lee, J. H. Kim, T. Hyeon, D. H. Kim, *Adv. Mater.* **2022**, *34*, 2200980.
[10] S. H. Jeong, S. Zhang, K. Hjort, J. Hilborn, Z. G. Wu, *Adv. Mater.* **2016**, *28*, 5830.
[11] J. H. Cheng, J. Shang, S. J. Yang, J. B. Dou, X. H. Shi, X. Y. Jiang, *Adv. Funct. Mater.* **2022**, *32*, 2200444.
[12] a) L. Qi, C. Ruck, G. Spychalski, B. King, B. X. Wu, Y. Zhao, *ACS Appl. Mater. Interfaces* **2018**, *10*, 4295; b) M. Parmeggiani, P. Zaccagnini, S. Stassi, M. Fontana, S. Bianco, C. Nicosia, C. F. Pirri, A. Lamberti, *ACS Appl. Mater. Interfaces* **2019**, *11*, 33221; c) V. Nair, J. Yi, D. Isheim, M. Rotenberg, L. Y. Meng, F. Y. Shi, X. Q. Chen, X. Gao, A. Prominski, Y. W. Jiang, J. P. Yue, C. T. Gallagher, D. N. Seidman, B. Z. Tian, *Sci. Adv.* **2020**, *6*, eaaz2743.
[13] H. Wang, Z. Zhao, P. Liu, X. Guo, *Theor. Appl. Mech. Lett.* **2021**, *11*, 100240.
[14] L. Yang, H. Ji, C. Meng, Y. Li, G. Zheng, X. Chen, G. Niu, J. Yan, Y. Xue, S. Guo, H. Cheng, *ACS Appl. Mater. Interfaces* **2022**, *14*, 17818.
[15] E. J. Heller, Y. Yang, L. Kocia, W. Chen, S. A. Fang, M. Borunda, E. Kaxiras, *ACS Nano* **2016**, *10*, 2803.
[16] A. Dallinger, K. Keller, H. Fitzek, F. Greco, *ACS Appl. Mater. Interfaces* **2020**, *12*, 19855.
[17] a) C. Zhang, Z. X. Peng, C. L. Huang, B. W. Zhang, C. Xing, H. M. Chen, H. Y. Cheng, J. Wang, S. L. Tang, *Nano Energy* **2021**, *81*, 105609; b) B. H. Sun, R. N. McCay, S. Goswami, Y. D. Xu, C. Zhang, Y. Ling, J. Lin, Z. Yan, *Adv. Mater.* **2018**, *30*, 1804327.
[18] a) N. Martirosyan, M. Y. S. Kalani, *World Neurosurg.* **2011**, *76*, 485; b) Z. L. Huang, Y. F. Hao, Y. Li, H. J. Hu, C. H. Wang, A. Nomoto, T. S. Pan, Y. Gu, Y. M. Chen, T. J. Zhang, W. X. Li, Y. S. Lei, N. Kim, C. F. Wang, L. Zhang, J. W. Ward, A. Maralani, X. S. Li, M. F. Durstock, A. Pisano, Y. Lin, S. Xu, *Nat. Electron.* **2018**, *1*, 473.

[19] a) H. Lim, H. Kwon, H. Kang, J. E. Jang, H. J. Kwon, *Nat. Commun.* **2023**, *14*, 3114; b) X. Zheng, B. Jia, H. Lin, L. Qiu, D. Li, M. Gu, *Nat. Commun.* **2015**, *6*, 8433.
[20] L. Yang, N. Yi, J. Zhu, Z. Cheng, X. Y. Yin, X. Y. Zhang, H. L. Zhu, H. Y. Cheng, *J. Mater. Chem. A* **2020**, *8*, 6487.
[21] X. C. Huang, H. Li, J. Y. Li, L. B. Huang, K. M. Yao, C. K. Yiu, Y. M. Liu, T. H. Wong, D. F. Li, M. G. Wu, Y. Huang, Z. Gao, J. K. Zhou, Y. Y. Gao, J. Li, Y. L. Jiao, R. Shi, B. B. Zhang, B. F. Hu, Q. L. Guo, E. M. Song, R. Q. Ye, X. G. Yu, *Nano Lett.* **2022**, *22*, 3447.
[22] J. B. Zhang, C. H. Zhang, J. W. Sha, H. L. Fei, Y. L. Li, J. M. Tour, *ACS Appl. Mater. Interfaces* **2017**, *9*, 26840.
[23] F. Ershad, A. Thukral, J. P. Yue, P. Comeaux, Y. T. Lu, H. Shim, K. Sim, N. I. Kim, Z. Y. Rao, R. Guevara, L. Contreras, F. J. Pan, Y. C. Zhang, Y. S. Guan, P. Y. Yang, X. Wang, P. Wang, X. Y. Wu, C. J. Yu, *Nat. Commun.* **2020**, *11*, 3823.
[24] L. Q. Zhang, L. Wang, J. Y. Li, C. Cui, Z. Q. Zhou, L. Y. Wen, *Nano Lett.* **2022**, *8*, 5451.
[25] L. Yang, J. Y. Yan, C. Z. Meng, A. Dutta, X. Chen, Y. Xue, G. Y. Niu, Y. Wang, S. J. Du, P. Zhou, C. Zhang, S. J. Guo, H. Y. Cheng, *Adv. Mater.* **2023**, *35*, 13.
[26] R. Rahimi, M. Ochoa, A. Tarnayol, S. Khalili, A. Khademhosseini, B. Ziaie, *ACS Appl. Mater. Interfaces* **2017**, *9*, 9015.
[27] a) A. A. Karyakin, *Curr. Opin. Electrochem.* **2017**, *5*, 92; b) F. Ricci, G. Palleschi, *Biosens. Bioelectron.* **2005**, *21*, 389.
[28] Y. Matos-Peralta, M. Antuch, *J. Electrochem. Soc.* **2019**, *167*, 037510.
[29] V. Anandan, X. Yang, E. Kim, Y. L. Rao, G. Zhang, *J. Biol. Eng.* **2007**, *1*, 5.
[30] a) X. Hui, X. Xuan, J. Kim, J. Y. Park, *Electrochim. Acta* **2019**, *328*, 135066; b) F. N. Zhao, J. W. He, X. J. Li, Y. P. Bai, Y. B. Ying, J. F. Ping, *Biosens. Bioelectron.* **2020**, *170*, 112636; c) Y. Luo, B. C. Zhu, S. Y. Zhang, P. K. Zhang, X. Li, L. Wang, B. H. Lu, J. Travas-Sejdic, *Adv. Mater. Technol.* **2022**, *7*, 2101571.
[31] J. Zhu, Z. H. Hu, C. Y. Song, N. Yi, Z. Z. Yu, Z. D. Liu, S. B. Liu, M. J. Wang, M. G. Dexheimer, J. Yang, H. Y. Cheng, *Mater. Today Phys.* **2021**, *18*, 100377.
[32] J. Kim, A. Banks, H. Cheng, Z. Xie, S. Xu, K.-I. Jang, J. W. Lee, Z. Liu, P. Gutruf, X. Huang, P. Wei, F. Liu, K. Li, M. Dalal, R. Ghaffari, X. Feng, Y. Huang, S. Gupta, U. Paik, J. A. Rogers, **2015**, *11*, 906.
[33] J. Kim, P. Gutruf, A. M. Chiarelli, S. Y. Heo, K. Cho, Z. Q. Xie, A. Banks, S. Han, K. I. Jang, J. W. Lee, K. T. Lee, X. Feng, Y. G. Huang, M. Fabiani, G. Gratton, U. Paik, J. A. Rogers, *Adv. Funct. Mater.* **2017**, *27*, 1604373.
[34] a) G. Xu, Y. L. Lu, C. Cheng, X. Li, J. Xu, Z. Y. Liu, J. L. Liu, G. Liu, Z. H. Shi, Z. T. Chen, F. N. Zhang, Y. X. Jia, D. F. Xu, W. Yuan, Z. Cui, S. S. Low, Q. J. Liu, *Adv. Funct. Mater.* **2021**, *31*, 2100852; b) D. Svirskis, M. Sharma, Y. Yu, S. Garg, *Ther. Delivery* **2013**, *4*, 307; c) S. Geetha, C. R. K. Rao, M. Vijayan, D. C. Trivedi, *Anal. Chim. Acta* **2006**, *568*, 119.
[35] Q. Pang, D. Lou, S. J. Li, G. M. Wang, B. B. Qiao, S. R. Dong, L. Ma, C. Y. Gao, Z. H. Wu, *Adv. Sci.* **2020**, *7*, 1902673.
[36] M. L. Goodwin, *J. Diabetes Sci. Technol.* **2010**, *4*, 694.
[37] K. F. Petersen, T. Price, G. W. Cline, D. L. Rothman, G. I. Shulman, *Am. J. Physiol.-Endocrinol. Metab.* **1996**, *270*, E186.
[38] Z. Peng, X. Xie, Q. Tan, H. Kang, J. Cui, X. Zhang, W. Li, G. Feng, **2022**, *15*, 2230003.
[39] A. Wiorek, M. Parrilla, M. Cuartero, G. A. Crespo, *Anal. Chem.* **2020**, *92*, 10153.